*Chin. Ann. Math.*
36B(5), 2015, 829–842
DOI: 10.1007/s11401-015-0983-8

**Chinese Annals of Mathematics, Series B**


# Pressure Boundary Conditions for Blood Flows

Kirill P. GOSTAF[1] Olivier PIRONNEAU[2]

(*In Honor of the Scientific Contributions of Professor Luc Tartar*)

**Abstract** Simulations of blood flows in arteries require numerical solutions of fluid-structure interactions involving Navier-Stokes equations coupled with large displacement visco-elasticity for the vessels.

Among the various simplifications which have been proposed, the surface pressure model leads to a hierarchy of simpler models including one that involves only the pressure. The model exhibits fundamental frequencies which can be computed and compared with the pulse. Yet unconditionally stable time discretizations can be constructed by combining implicit time schemes with Galerkin-characteristic discretization of the convection terms in the Navier-Stokes equations. Such problems with prescribed pressure on the walls will be shown to be efficient and accurate as an approximation of the full fluid structure interaction problem.

**Keywords** Fluid-structure interaction, Compliant walls, Finite element method, Navier-Stokes equations, Blood flow
**2000 MR Subject Classification** 35Q30, 74K25, 65M60, 65N12

## 1 Introduction

Computational hemodynamics is a major research field with many applications to the human blood circulatory system (especially for heart diseases and aneurysms) leading to diagnostic tools and simulations of chirurgical treatments like stents (see [34]) and by-passes (see [35]).

Since the pioneering work of Peskin [27] impressive progress was made both on the methodological side, namely the treatment of moving walls, cardiac muscles, etc., and on the numerical side for efficient and stable discretizations of these fluid structure interaction problems. Some were presented in [13], mostly with methods on fixed domains after a change of variables (see [7, 12, 24] and the reference therein). For other methods like the fictitious domain and immersed boundary methods, the reader is referred to [2, 26–27, 36], among others. Level sets have not been as popular but they can also be used as in [5].

In this paper, we focus on geometries similar to aortic flows. Typically, a large artery like the aorta has a radius of 1cm and a length of 5 to 10 centimeters; the thickness of the aortic wall is around 0.1 cm; the heart pulse is about 1 Hz and the pressure at the input boundary

Manuscript received August 8, 2014.
[1]Department of Mathematics, Simon Fraser University, Burnaby V5A 1S6, BC, Canada. E-mail: gostaf@sfu.ca
[2]Laboratoire Jacques-Louis Lions, Université Pierre et Marie Curie, Place Jussieu, Boite 187, Paris 75252, France. E-mail: Olivier.Pironneau@upmc.fr

6KPa. Knowing the density and viscosity, this fixes a typical speed for the blood. At such speed the flow is Newtonian, incompressible with a Reynolds number of a few thousand.

The aorta is surrounded by organs, so in all its generality the problem is very complex: Large displacement visco-elasticity deformable solid with contacts on the surrounding organs and fluid-structure interaction (FSI for short) with a flow modeled by the Navier-Stokes equations in a moving domain.

## 2 Modeling the Aortic Wall: The Surface Pressure Model

The modeling and simulations of solids having large displacements and contacts are difficult but not impossible (see [16–17]), and rubber tires in particular are modeled as such, but they are computationally very expensive and even more so in the context of blood flow (see the computations in [23]).

A hierarchy of approximations was proposed. First, replace large displacement nonlinear elasticity by small displacement linear elasticity (see [6]), then use shell models like Koiter's as in [8, 22], and finally assume that the displacement $\vec{d}$ is normal to the aortic wall,

$$\vec{d}(x,t) = \eta(x,t)\vec{n}(x).$$

In such case, as shown in [24], Koiter's model reduces to a scalar equation for $\eta$,

$$\rho^{\rm s} h\partial_{tt}\eta - \nabla\cdot(\mathbf{T}\nabla\eta) - \nabla\cdot(\mathbf{C}\nabla\partial_t\eta) + a\partial_t\eta + b\eta = f^{\rm s} \quad \text{for } \eta,\ \partial_t\eta \text{ given at } t=0 \tag{2.1}$$

on the mean position $\Sigma$ of the vessel's wall, where $h$ denotes its average thickness and $\rho^{\rm s}$ its density, $\mathbf{T}$ is the pre-stress tensor, needed because at rest the vessel is blown up by the blood like a balloon, $\mathbf{C}$ is a damping term, $a, b$ are viscoelastic terms, and $f^{\rm s}$ is the external normal force, i.e., $-\sigma^{\rm s}_{nn}$ is the normal component of the normal stress at the surface of the solid.

The final approximation is to assume that $[h, T, C, a] \ll b$ which leads to the surface pressure model

$$-\sigma^{\rm s}_{nn} = b\eta \quad \text{with } b = \frac{Eh\pi}{A(1-\xi^2)}, \tag{2.2}$$

where $A$ is the vessel's cross section, $E$ is the Young modulus, and $\xi$ is the Poisson coefficient. Some typical values (MKSA for short) are as follows:

$$E = 3\,\text{MPa},\ \xi = 0.3,\ A = \pi R^2,\ R = 0.01,\ h = 0.001 \Rightarrow b = 3.3\times 10^7\,\text{ms}^{-2}. \tag{2.3}$$

(2.2) assumes a circular cross section, but it can be extended to other shapes (see [24]).

## 3 Modeling Fluids with Given Boundary Pressure or Stress

For Newtonian incompressible fluids, pressure $p$ and velocity $\vec{u}$ are given by

$$\rho^{\rm f}\Big(\frac{\partial\vec{u}}{\partial t} + \vec{u}\cdot\nabla\vec{u}\Big) + \nabla\cdot\sigma^{\rm f} = 0, \quad \nabla\cdot\vec{u} = 0, \tag{3.1}$$

where $\rho^{\mathrm{f}}$ is the density of the fluid, $\mu$ is the viscosity and $\sigma^{\mathrm{f}} = -p\mathbf{I} + \mu(\nabla u + \nabla u^{\mathrm{T}})$ is the stress tensor.

Many boundary conditions were proposed for the artificial boundaries created by taking only a portion of the blood circulatory system (see [10, 12, 37]).

In this paper, the velocity and pressure are given at time $t = 0$, the pressure is given on $\Gamma$ (the inlet and the outlet) and the normal stress is given on $\Sigma$ by the structure model for the compliant wall. Naturally, $\Gamma \cup \Sigma = \partial\Omega$. As the inlet and outlet are artificial boundaries, we assume that $\Gamma$ is made of plane surfaces and the flow is normal to the inlet and outlet (the butcher cuts perpendicularly to the vessel), and the surface pressure model also implies normal velocity on $\Sigma$,

$$u|_{t=0} = u^0, \quad \vec{u} \times \vec{n} = 0 \quad \text{on } \partial\Omega, \quad p|_\Gamma = p_\Gamma, \quad \sigma^{\mathrm{f}}_{nn} = s \quad \text{on } \Sigma. \tag{3.2}$$

A variational formulation is obtained by multiplying the first equation in (3.1) by $\widehat{u}$ and the second one by $\widehat{p}$. Then for all $\widehat{p}$ and all $\widehat{u}$ such that $\widehat{u} \times n = 0$ on $\partial\Omega$,

$$\begin{aligned} &\int_\Omega \Big[\rho^{\mathrm{f}}(\partial_t u \cdot + u \cdot \nabla u) \cdot \widehat{u} + \frac{\mu}{2}(\nabla u + \nabla u^{\mathrm{T}}) : (\nabla \widehat{u} + \nabla \widehat{u}^{\mathrm{T}}) - p\nabla \cdot \widehat{u} - \widehat{p}\,\nabla \cdot u\Big] \\ &= \int_{\partial\Omega} \sigma^{\mathrm{f}}_{nn} \widehat{u}_n = \int_\Sigma s\widehat{u}_n - \int_\Gamma p_\Gamma \widehat{u}_n, \end{aligned} \tag{3.3}$$

where $\widehat{u}_n := \widehat{u} \cdot n$. Indeed, when $\Gamma$ is flat,

$$u \times n = 0, \ \nabla \cdot u = 0 \Rightarrow \sigma^{\mathrm{f}}_{nn} = -p,$$

because the tangential derivatives of $u$ are zero.

Such pressure boundary conditions were studied in [1, 29] (see also [28]). Existence and uniqueness may be proved as in the classical case following [15], and finite element approximations have been studied in [25], but there are some difficulties. First, because of the condition $u \times n|_{\partial\Omega} = 0$, one aught to use the curl-curl formulation,

$$\int_\Omega [(\partial_t u \cdot + u \cdot \nabla u) \cdot \widehat{u} + \mu \nabla \times u \cdot \nabla \times \widehat{u} - p\nabla \cdot \widehat{u} - \widehat{p}\nabla \cdot u] = \int_\Sigma s\widehat{u}_n - \int_\Gamma p_\Gamma \widehat{u}_n, \quad \forall \widehat{u}, q.$$

Recovery of the strong form of the Navier-Stokes equations when regularity allows makes use of the following formula (see [3–4]): For all $u, v \in H^2(\Omega)$ with either $u \times n = v \times n = 0$ or $u \cdot n = v \cdot n = 0$ on $\partial\Omega$,

$$\begin{aligned} &\int_\Omega [\nabla \times u \cdot \nabla \times v + \nabla \cdot u \ \nabla \cdot v] \\ &= \int_\Omega \nabla u : \nabla v + b(u, v) = \int_\Omega \Big[\frac{1}{2}(\nabla u + \nabla u^{\mathrm{T}}) : (\nabla v + \nabla v^{\mathrm{T}}) - \nabla \cdot u \ \nabla \cdot v\Big] + 2b(u, v) \end{aligned} \tag{3.4}$$

with $b(u, v) = \int_{\partial\Omega}[((u - u_n\, n) \cdot \nabla n) \cdot (v - v_n n) + u_n(\nabla \cdot n)v_n]$. Furthermore, if $\partial\Omega$ is piecewise plane, then

$$\begin{aligned} &\int_\Omega [\nabla \times u \cdot \nabla \times v + \nabla \cdot u \ \nabla \cdot v] \\ &= \int_\Omega \nabla u : \nabla v = \int_\Omega \Big[\frac{1}{2}(\nabla u + \nabla u^{\mathrm{T}}) : (\nabla v + \nabla v^{\mathrm{T}}) - \nabla \cdot u \ \nabla \cdot v\Big]. \end{aligned} \tag{3.5}$$

To summarise, the curl-curl formulation is the one supported by the theory while (3.3) is the one that the practioner demands, but they are equivalent in the context of the surface pressure model because $u \times n = 0$ on the $\partial\Omega$.

## 4 The Fluid-Structure Interaction Problem

### 4.1 Variational form of the model for $[\vec{u}, p, \eta]$

Coupling the two systems of (2.2)–(3.3) and writing the continuity of the velocities at the interface $\Sigma$, namely, $\vec{u} = \partial_t \vec{d} \approx \vec{n}\partial_t\eta$, lead to finding $[\vec{u}, p, \eta]$ with $u \times n = 0$, $\eta|_\Gamma = 0$ and

$$\int_\Omega \Big[\rho^{\rm f}(\partial_t u \cdot + u \cdot \nabla u) \cdot \widehat{u} + \frac{\mu}{2}(\nabla u + \nabla u^{\rm T}) : (\nabla\widehat{u} + \nabla\widehat{u}^{\rm T}) - p\nabla\cdot\widehat{u} - \widehat{p}\nabla\cdot u\Big]$$
$$+ \int_\Sigma b[\eta\widehat{u}_n + \widehat{\eta}(u_n - \partial_t\eta)] = -\int_\Gamma p_\Gamma \widehat{u}_n, \quad \forall\widehat{u}, \widehat{p}, \widehat{\eta} \text{ with } \widehat{u} \times n = 0,\ \widehat{\eta}|_\Gamma = 0. \tag{4.1}$$

It must be noted that $\Omega$ and its boundary are functions of time and must be updated by the displacement $\vec{d}$ as in [11]. As it is unfeasible to move $\Gamma$, we assume that $\eta|_\Gamma = 0$.

An energy conservation identity is obtained as follows by letting $\widehat{u} = u$, $\widehat{p} = -p$ and $\widehat{\eta} = -\eta$:

$$\int_\Omega \Big[\rho^{\rm f}\partial_t u \cdot u + \frac{\mu}{2}|\nabla u + \nabla u^{\rm T}|^2\Big] + \int_{\partial\Omega}\Big[\frac{u_n}{2}\rho^{\rm f}|u|^2 + b\eta\partial_t\eta\Big] = -\int_\Gamma p_\Gamma u_n. \tag{4.2}$$

Making use of the identity

$$\partial_t \int_{\Omega(t)} \frac{|u|^2}{2} = \int_{\Omega(t)} \partial_t u \cdot u + \int_{\partial\Omega(t)} \frac{u_n}{2}|u|^2$$

when the boundary moves with speed $u_n$, we come to

$$\int_{\Omega(T)} \rho^{\rm f}\frac{|u|^2}{2} + \int_0^{\rm T}\int_{\Omega(t)} \frac{\mu}{2}|\nabla u + \nabla u^{\rm T}|^2 + \int_{\Sigma(T)} \frac{b}{2}\eta^2$$
$$= \int_{\Omega(0)} \rho^{\rm f}\frac{|u|^2}{2} + \int_{\Sigma(0)} \frac{b}{2}\eta^2 - \int_0^{\rm T}\int_\Gamma \Big(p_\Gamma + \frac{\rho^{\rm f}}{2}|u|^2\Big)u_n. \tag{4.3}$$

Thus kinetic energy decreases due to viscosity when $\Gamma = \emptyset$.

The curl-curl low Reynolds approximation of (4.1) consists in finding $[u, p, \eta]$ with $u \times n|_{\partial\Omega} = 0$, $\eta|_\Gamma = 0$ and

$$\int_\Omega [\rho^{\rm f}\partial_t u \cdot \widehat{u} + \mu\nabla\times u \cdot \nabla\times\widehat{u}^{\rm T} - p\nabla\cdot\widehat{u} - \widehat{p}\nabla\cdot u] + \int_\Sigma b[\eta\widehat{u}_n + \widehat{\eta}(u_n - \partial_t\eta)]$$
$$= -\int_\Gamma p_\Gamma\widehat{u}_n, \quad \widehat{u}\times n = 0,\ \widehat{\eta}|_\Gamma = 0,\ \forall\widehat{u}, \widehat{p}, \widehat{\eta}. \tag{4.4}$$

Following [14], existence and uniqueness can be shown, subject to the regularity hypotheses, because the bilinear form $[u, \widehat{u}] \to \int_\Omega \nabla\times u \cdot \nabla\times\widehat{u}$ is strongly elliptic in the appropriate space of curl free vector fields and the bilinear form $[(p, \eta), \widehat{u}] \to -\int_\Omega p\nabla\cdot\widehat{u} + b\int_\Sigma \eta\widehat{u}_n$ satisfies the inf-sup condition.

## 5 A Hierarchy of Approximations on Fixed Domains

First note that $\sigma_{nn}|_\Gamma \approx -p$, because $\mu$ is small and $\nabla u \approx \mathbf{I}\partial_n u_n \approx 0$ due to $u \times n = 0$. Therefore, at the moving wall $\Sigma$,

$$p = b\eta,\ u_n = \partial_t \eta \Rightarrow b u_n = \partial_t p. \tag{5.1}$$

To simplify notations let us work with the reduced pressure $\frac{p}{\rho^{\mathrm{f}}}$. Then with $b \to \frac{b}{\rho^{\mathrm{f}}}$, (5.1) is unchanged.

Now recall the concept of transpiration condition (see [9, 28]). Instead of applying a boundary condition on a wall $\Sigma(t)$ moving normally by $\eta(x,t)$, we shall apply it on a fixed wall $\Sigma$ with a correction factor based on the following:

$$u(x+\eta\vec{n}) = \vec{n}\frac{\partial \eta}{\partial t}(x),\ x \in \Sigma(t) \Leftrightarrow u + \eta\frac{\partial u}{\partial n} = \vec{n}\frac{\partial \eta}{\partial t} + o(\eta),\ x \in \Sigma(t).$$

If the radius of curvature of $\Sigma$ is large and if $u \times n|_{\partial\Omega} = 0$, then, as said earlier,

$$n \cdot \frac{\partial u}{\partial n} \approx \frac{\partial u_n}{\partial n} \approx \nabla \cdot u - \frac{\partial u_s}{\partial s} - \frac{\partial u_\tau}{\partial \tau} = 0$$

implying that the transpiration correction is of higher order.

So instead of (4.1), a simpler formulation is obtained after distcretization in time and on a fixed domain. Together with (5.1), we must then solve (5.2) below.

### 5.1 A model with velocity and pressure only

Consider the following problem.

Find $[u^{m+1}, p^{m+1}]$ with $u^{m+1} \times n = 0$ and $\forall \widehat{u}$, $\widehat{p}$ with $\widehat{u} \times n = 0$, with

$$\begin{aligned}&\int_\Omega \Big[\widehat{u} \cdot \Big(\frac{u^{m+1}-u^m}{\delta t} - u^{m+\frac{1}{2}} \times \nabla \times u^m\Big) - p^{m+1}\nabla \cdot \widehat{u} - \widehat{p}\,\nabla \cdot u^{m+\frac{1}{2}}\Big] \\ &+ \int_\Omega \nu \nabla \times u^{m+\frac{1}{2}} \cdot \nabla \times \widehat{u} + \int_\Sigma (u^{m+\frac{1}{2}} b\delta t + p^m \vec{n}) \cdot \widehat{u} = -\int_\Gamma p_\Gamma \widehat{u}_n.\end{aligned} \tag{5.2}$$

We use the identity: $u \cdot \nabla u = -u \times \nabla \times u + \nabla \frac{|u|^2}{2}$, and we remove the last term which is compensated by the moving domain in (4.1) and which ought to be absent in the fixed domain model to preserve energy (an approximation of order 2 in $u_n|_\Sigma$), assumed small from the start. Indeed, integration by parts leads to

$$\begin{aligned}&\frac{u^{m+1}-u^m}{\delta t} - u^{m+\frac{1}{2}} \times \nabla \times u^m + \nabla p^{m+1} + \nu \nabla \times \nabla \times u^{m+\frac{1}{2}} = 0, \quad \nabla \cdot u^{m+1} = 0, \\ &u^{m+\frac{1}{2}} b\delta t + p^m \vec{n} - p^{m+1}\vec{n} = 0.\end{aligned}$$

Then, in the case $\Gamma = \emptyset$, an energy estimate is obtained by letting $\widehat{u} = u^{m+\frac{1}{2}}$ and $\widehat{p} = -p^{m+1}$ in (5.2), which leads to the following identity:

$$\begin{aligned}&\int_\Omega |u^{m+1}|^2 + \nu\delta t \sum_{k\le m} \int_\Omega |\nabla \times u^{k+\frac{1}{2}}|^2 + \frac{\delta t}{2b} \sum_{k<m} \int_{\partial\Omega} \Big(\frac{p^{k+1}-p^k}{\delta t}\Big)^2 + \frac{1}{2b\delta t}\int_{\partial\Omega} {p^{m+1}}^2 \\ &= \int_\Omega |u^0|^2 + \frac{1}{2b\delta t}\int_{\partial\Omega} {p^0}^2.\end{aligned} \tag{5.3}$$

### 5.2 A model involving only the pressure

In a strong form, (5.2) is

$$\begin{aligned}
&\partial_t u - u\times\nabla\times u + \nabla p - \nu\Delta u = 0, \quad \nabla\cdot u = 0,\\
&u|_{t=0} = u^0 \quad \text{in } \Omega,\\
&b\vec{u} = \vec{n}\partial_t p|_\Sigma \quad \text{or} \quad \vec{u}\times\vec{n}|_\Gamma = 0, \quad p|_\Gamma = p_\Gamma.
\end{aligned} \tag{5.4}$$

Taking the divergence of the PDE and its scalar product with $n$ leads to

$$\begin{aligned}
&-\Delta p = -\nabla\cdot(u\times\nabla\times u) \quad \text{in } \Omega,\\
&\frac{\partial p}{\partial n}|_\Sigma = \nu\Delta u\cdot n - \partial_t u\cdot n = \nu\Delta u\cdot n - \frac{1}{b}\partial_{tt} p, \quad p|_\Gamma = p_\Gamma.
\end{aligned} \tag{5.5}$$

Note that it could also be found from (5.2) by choosing $\widehat{u} = \nabla q$ and $\widehat{p} = 0$.

When $u\times\nabla\times u$ and $\nu\Delta u\cdot n|_\Sigma$ are small, an autonomous equation for $p$ is

$$-\Delta p = 0 \text{ in } \Omega,\ \partial_{tt} p + b\frac{\partial p}{\partial n} = 0 \text{ on } \Sigma \Rightarrow \partial_{tt} p_\Sigma - b\Delta_\Sigma p_\Sigma = 0, \tag{5.6}$$

where $-\Delta_\Sigma$ is the Steklov-Poincaré operator $p|_\Gamma \to \frac{\partial p}{\partial n}|_\Gamma$ via $\Delta p = 0$.

Two comments:

(1) While $\nu\Delta u\cdot n|_\Sigma$ is generally small for aortic flow, $u\times\nabla\times u$ may not be; except when the flow is irrotational, which is the case only if the flow is nearly the Poiseuille pipe flow. So (5.6) is clearly only a first approximation to the problem.

(2) Resonance may occur in (5.6) at $\sqrt{b\lambda_{(-\Delta_\Sigma)}}$, which is an important observation that could explain why the full problem on a moving domain is so hard and algorithms nearly unstable.

Resonance is due to the finite length of the aortic geometry used in the computation.

To estimate the resonance frequency is easy in 2D: Take a rectangle $(0, L)\times(-R, R)$ and the data in (2.3).

If $p(x, y) = f(x)g(y)$, then $-\Delta p = 0$ leads to $f'' + a^2 f = 0,\ -g'' + a^2 g = 0$, as $g$ is maximum at $y = 0$, $g = \cosh(ay)$, and thus $g'(R) = a\sinh(aR)$.

Similarly, as $f(0) = f(L) = 0$, $f = \sin(ax)$ with the necessary condition that $aL = k\pi,\ k \in N^+$. So the eigenvalue problem is

$$-\lambda^2 p(x, R) + b\partial_y p(x, R) = 0 \Rightarrow \lambda^2 = ba\tanh(aR). \tag{5.7}$$

When $aR$ is small, $\lambda \approx \frac{k\pi}{L}\sqrt{bR}$, so the first eigenvalue is $\lambda_1 = 0.9\,\text{cm}$.

## 6 Discretization with a Finite-Element Method

Let $T_h$ be a triangulation with $K$ tetrahedra $\{T_k\}_1^K$ under the usual conformity hypotheses, and let $\Omega := \bigcup_k T_k \subset \mathbb{R}^3$.

Consider the $P^2 - P^1$ element built from

$$\begin{aligned}
V_h &= \{v \in C^0(\overline{\Omega})^3 : v_i|_{T_k} \in P^2,\ i = 1, 2, 3\},\\
Q_h &= \{q \in C^0(\overline{\Omega}) : q|_{T_k} \in P^1\}.
\end{aligned} \tag{6.1}$$

### 6.1 Discretization of the full problem (4.1)

A feasible discretization of (4.1) is to find $[u^{m+1}, p^{m+1}, \eta^{m+1}] \in V_h \times Q_h \times Q_h$ with $u^{m+1} \times n|_\Gamma = 0$, $\eta^{m+1}|_\Gamma = 0$ such that

$$\begin{aligned}
&\int_\Omega \Big[\widehat{u} \cdot \Big(\frac{u^{m+1} - u^m}{\delta t} - u^{m+\frac{1}{2}} \times \nabla \times u^m\Big) - p^{m+1} \nabla \cdot \widehat{u} - \widehat{p} \nabla \cdot u^{m+\frac{1}{2}} \\
&+ \frac{\nu}{2}(\nabla u^{m+\frac{1}{2}} + \nabla u^{m+\frac{1}{2}^{\mathrm{T}}}) : (\nabla \widehat{u} + \nabla \widehat{u}^{\mathrm{T}}) + \varepsilon \nabla \eta^{m+\frac{1}{2}} \cdot \nabla \widehat{\eta} + \frac{1}{\epsilon} \nabla \times u^{m+\frac{1}{2}} \cdot \nabla \times \widehat{u}\Big] \\
&+ \int_\Sigma b\Big[\eta^{m+\frac{1}{2}} \widehat{u}_n - \widehat{\eta}\Big(u_n^{m+\frac{1}{2}} - \frac{1}{\delta t}(\eta^{m+1} - \eta^m)\Big)\Big] \\
&= -\int_\Gamma p_\Gamma \widehat{u}_n, \quad \forall [\widehat{u}, \widehat{p}, \widehat{\eta}] \in V_h \times Q_h \times Q_h \text{ with } \widehat{u} \times n|_{\partial\Omega} = 0,\ \widehat{\eta}|_\Gamma = 0,
\end{aligned} \tag{6.2}$$

where $\varepsilon$ is any small positive parameter.

When $\Omega$ is kept fixed, an energy conservation identity is found by choosing $\widehat{u} = u^{m+\frac{1}{2}}$, $\widehat{p} = -p^{m+1}$ and $\widehat{\eta} = \eta^{m+\frac{1}{2}}$,

$$\begin{aligned}
&\int_\Omega \Big(\frac{u^{m+1^2} - u^{m^2}}{2\delta t} + \frac{\nu}{2}|\nabla u^{m+\frac{1}{2}} + \nabla u^{m+\frac{1}{2}^{\mathrm{T}}}|^2 + \varepsilon |\nabla \eta^{m+\frac{1}{2}}|^2 + \frac{1}{\epsilon}|\nabla \times u^{m+\frac{1}{2}}|^2\Big) \\
&+ \int_\Sigma \frac{\eta^{m+1^2} - \eta^{m^2}}{2\delta t} = -\int_\Gamma p_\Gamma \widehat{u}_n^{m+\frac{1}{2}}.
\end{aligned} \tag{6.3}$$

As for the Navier-Stokes equations, when $\delta t$ is small enough, the problem has a unique solution because of the energy estimate and because of a general inf-sup condition is satisfied with $p$ replaced by $[p, \eta]$.

### 6.2 Discretization of problem (5.2) in $[\boldsymbol{u}, \boldsymbol{p}]$

A feasible discretization of (5.2) is to find $u^{m+1} \in V_h,\ p^{m+1} \in Q_h$ with $u^{m+1} \times n|_\Gamma = 0$ and such that

$$\begin{aligned}
&\int_\Omega \Big[\widehat{u} \cdot \Big(\frac{u^{m+1} - u^m}{\delta t} - u^{m+\frac{1}{2}} \times \nabla \times u^m\Big) - p^{m+1} \nabla \cdot \widehat{u} - \widehat{p} \nabla \cdot u^{m+\frac{1}{2}}\Big] \\
&+ \int_\Omega \Big[\frac{\nu}{2}(\nabla u^{m+\frac{1}{2}} + \nabla u^{m+\frac{1}{2}^{\mathrm{T}}}) : (\nabla \widehat{u} + \nabla \widehat{u}^{\mathrm{T}}) + \frac{1}{\epsilon} \nabla \times u^{m+\frac{1}{2}} \cdot \nabla \times \widehat{u} \\
&+ \nu \nabla \times u^{m+\frac{1}{2}} \cdot \nabla \times \widehat{u}\Big] + \int_\Sigma (u^{m+\frac{1}{2}} b \delta t + p^m \vec{n}) \cdot \widehat{u} \\
&= -\int_\Gamma p_\Gamma \widehat{u}_n, \quad \forall \widehat{u} \in V_h,\ \widehat{p} \in Q_h \text{ with } \widehat{u} \times n|_\Gamma = 0.
\end{aligned} \tag{6.4}$$

When $\Gamma$ is flat and perpendicular to an axis, $u^{m+1} \times n|_\Gamma = 0$ amounts to some component of the velocity being zero; it is easy to implement. If not, then it must be added by penalty in the variational formulation.

The difference to a standard Stokes problem is only the added integral on $\Sigma$ which reinforces the ellipticity of the bilinear form. Thanks to the inf-sup condition, the problem is well-posed. Error estimates, however, need to be rederived.

Notice that the energy equality does not imply stability,

$$\int_\Omega \Big[\frac{u^{m+1^2} - u^{m^2}}{2\delta t} + \nu |\nabla \times u^{m+\frac{1}{2}}|^2\Big] + \int_\Sigma [b|u^{m+\frac{1}{2}}|^2 \delta t + p^m u_n^{m+\frac{1}{2}}] = -\int_\Gamma p_\Gamma \widehat{u}_n^{m+\frac{1}{2}}. \tag{6.5}$$

### 6.3 Stability

For a high Reynolds number, some upwinding must be applied. Then it is easier to revert to $u \cdot \nabla u$ for the nonlinear term and to use the Characteristic-Galerkin method (see [30, 33] for a second order version). At each time step, one seeks for $u^{m+1} \in V_h,\ p^{m+1} \in Q_h$ with $u^{m+1} \times n|_\Gamma = 0$ and

$$\int_\Omega \Big[\widehat{u} \cdot \Big(\frac{u^{m+1} - u^m \circ X^m}{\delta t}\Big) - p^{m+1}\nabla \cdot \widehat{u} - \widehat{p}\nabla \cdot u^{m+1}\Big] + \int_\Omega \nu \nabla \times u^{m+1} \nabla \times \widehat{u}$$
$$+ b\delta t \int_\Sigma u^{m+1} \cdot \widehat{u} = \int_\Gamma p_\Gamma \widehat{u}_n - \int_\Sigma p^m \widehat{u}_n, \quad \forall \widehat{u} \in V_h,\ \widehat{p} \in Q_h \text{ with } \widehat{u} \times n|_\Gamma = 0, \tag{6.6}$$

where $X^m(x)$ is a first-order volume preserving (because $\nabla \cdot u^m \approx 0$) approximation of the solution at $t^m$ of

$$\dot{X}(\tau) = u^m(X(\tau), \tau), \quad X(t^{m+1}) = x. \tag{6.7}$$

To be equivalent to (6.4) an integral of ${u^{m+1}}^{\mathrm{T}} \nabla u \widehat{u}$ should be added to (6.6), but we know that this term ought to be neglected when we pass from a varying domain to a fixed domain. To preserve energy, we suggest to drop the term, which means that the formulation is valid approximately if and only if $u^m|_\Sigma$ is small.

Indeed, assuming no quadrature error and choosing $\widehat{u} = u^{m+1}$, $\widehat{p} = -p^{m+1}$ lead to

$$\frac{1}{\delta t}\|u^{m+1}\|_0^2 + \nu\|\nabla \times u^{m+1}\|_0^2 + b\delta t\|u^{m+1}\|_{0,\Sigma}^2$$
$$= \frac{1}{\delta t}\int_\Omega u^{m+1} \cdot u^m \circ X^m + \int_\Gamma p_\Gamma u^{m+1} - \int_\Sigma p^m u_n^{m+1}. \tag{6.8}$$

But again the last term seems hard to bound.

A similar use of the Characteristic-Galerkin method can be applied to (6.4) and there stability is not a problem, so though more expensive, (6.4) is mathematically a better formulation.

### 6.4 Discretization of (5.2) with operator decomposition

We can make explicit use of the boundary condition on the pressure and make a Chorin-like decomposition of (5.2). The following problems are solved in sequence:

$$\begin{aligned}
&-\Delta p^{m+1} = \nabla \cdot (u^m \circ X^m) \quad \text{in } \Omega,\\
&\frac{1}{\delta t^2}(p^{m+1} - 2p^m + p^{m-1}) + b\frac{\partial p^{m+1}}{\partial n} = 0 \quad \text{on } \Sigma, \quad p^{m+1}|_\Gamma = p_\Gamma,\\
&\frac{1}{\delta t}(u^{m+1} - u^m \circ X^m) + \nabla p^{m+1} - \nu\Delta u^{m+1} = 0 \quad \text{in } \Omega,\\
&u^{m+1}|_\Sigma = \frac{\vec{n}}{b\delta t}(p^{m+1} - p^m), \quad u^{m+1} \times n|_\Gamma = 0.
\end{aligned} \tag{6.9}$$

Parallel implementations could take advantage of such decomposition. However it is not clear that an iterative solution of the full system by block decomposition (see [6, 18]) is not faster than this Chorin-like decomposition. Second order decomposition should also be studied in this context (see [21, 31]).

### 6.5 Discretization of the pressure problem (5.6)

Alternatively, no such difficulty arises with the pressure equation (5.6). The following scheme, for instance, is stable with a fixed geometry:

$$\frac{1}{2}\int_\Omega \nabla(p^{m+1}+p^{m-1})\cdot\nabla\widehat{p}+\frac{1}{b}\int_\Sigma \widehat{p}\frac{p^{m+1}-2p^m+p^{m-1}}{\delta t^2}=0,$$
$$\forall\widehat{p}\in Q_h,\ \widehat{p}|_\Gamma=0,\ p^{m+1}\in Q_h,\ p^{m+1}|_\Gamma=p_\Gamma. \tag{6.10}$$

### 6.6 Moving the geometry for graphic visualization

The theory requires that $\Sigma$ be moved at every time step along its normal of a quantity $\delta t u^m\cdot\vec{n}$. To preserve the triangulation, we follow [9], solve an additional problem

$$-\Delta\vec{d}^{m+1}=0\quad\text{in }\Omega,\quad \vec{d}^{m+1}|_\Sigma=\vec{d}^m+\vec{n}\delta t u_n^m,\quad \vec{d}^{m+1}|_\Gamma=0, \tag{6.11}$$

and then move every vertex $q^j$ of the triangulation $q^j\to q^j+\kappa d$. In theory $\kappa=1$ but for graphic enhancement, it can be adjusted. Note however that (6.11) is expensive to solve.

## 7 Numerical Tests

### 7.1 Comparison of the four methods

We begin with a comparison of (6.2), (6.6) and (6.9)–(6.10) on a simple geometry: A quarter of a torus with a pressure drop imposed from the top horizontal cross section to the right vertical one. The geometry is not updated but moved for graphic rendering.

The cross section of the torus is a circle of radius 1 cm. This circle is extruded to a greater circle of radius 4 cm. The pressure drop is $6\cos(\pi t)$, $b=200$ and $\nu=0.001$. The time step is 0.05, voluntarily large to illustrate stability. The computation is stopped at $t=0.75$.

Figure 1 shows the pressure at $t=0.75$ by the four methods. It is seen that (6.2) and (6.6) give the same results. However while (6.9)–(6.10) agree with each other (an indication that $u\times\nabla\times u$ is small), they only agree qualitatively with (6.2). The computing time is given in Table 1.

Table 1 Computing time for (6.2), (6.6) and (6.9)–(6.10)

| Method | $[u,v,w,p,\eta]$ | $[u,v,w,p]$ | $p\to[u,v,w]$ | $p$ |
|---|---|---|---|---|
| CPU | 10.9 | 9.6 | 31.5 | 5.38 |

The linear systems are solved with the library UMFPACK which explains why (6.9) is so much more expensive. The mesh has 1395 vertices giving 6975 degrees of freedom for each linear system for $[u^{m+1},v^{m+1},w^{m+1},p^{m+1},\eta^{m+1}]$.

Figure 2 shows the values of $|u\times\nabla\times u|$ and $\nu n^{\mathrm{T}}(\nabla u)n$ when the flow is computed using the $[u,v,w,p]$ model. It is seen that $\nu n^{\mathrm{T}}(\nabla u)n$ is not small at the lower section while $\nu n^{\mathrm{T}}(\nabla u)n$ is small everywhere.

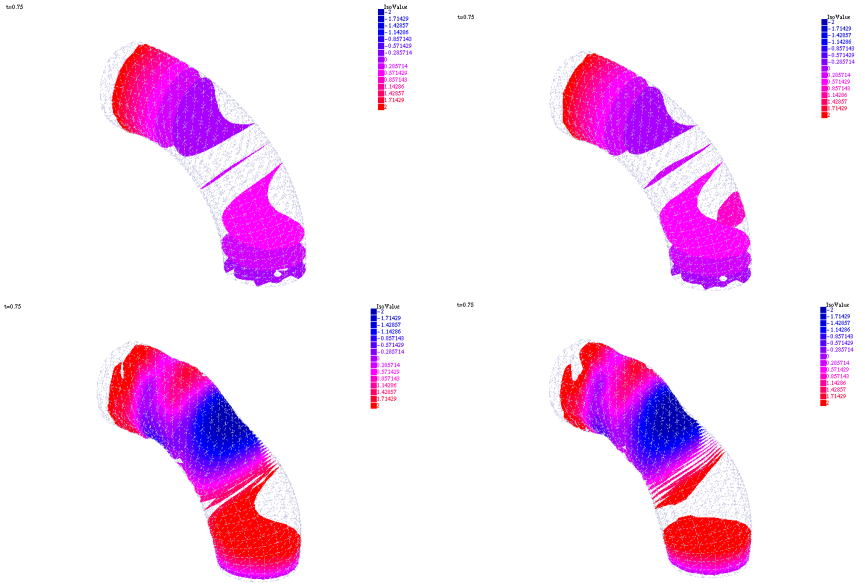

Figure 1 Top left: Computation of $[u, v, w, p, \eta]$ with (6.2). Top right: Computation of $[u, v, w, p]$ with (6.6). Bottom left: Computation of $[u, v, w, p]$ using operator decomposition (6.9). Bottom right: Computation of the pressure only $p$ with (6.10).

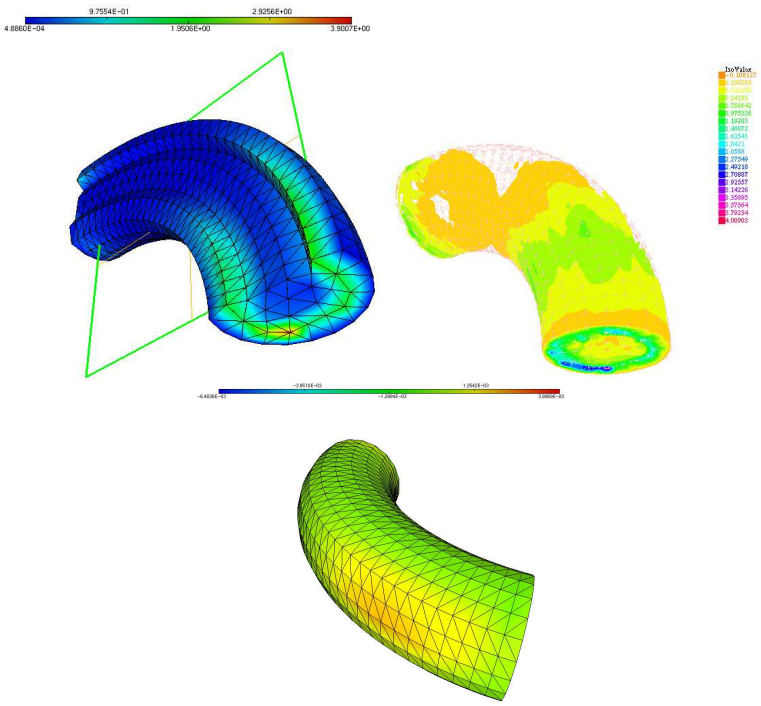

Figure 2 Top: Two views of $|u \times \nabla \times u|$. Bottom: $\nu n^{\mathrm{T}}(\nabla u)n$ on the wall of the vessel. The lower section of the tube faces the reader.

### 7.2 Performance for the aorta

The geometry is a section of the aorta obtained from an MRI scan. It has 4991 vertices, giving 19964 degrees of freedom for each linear system for $[u_1^{m+1}, u_2^{m+1}, u_3^{m+1}, p^{m+1}]$. The pressure drop from the inflow section on the right to the outflow section on the left is $p_{\Gamma_R} = 6\cos^2(\pi t)$ and the results are shown at $t = 0.8$. On the smaller cross sections, a pressure drop equal to $\frac{p_{\Gamma_R}}{2}$ is imposed. (6.6) is used with $\delta t = 0.05$, $\nu = 0.001$ and $b = 200$. The computation took $342''$ on a macbook pro $15''$, 2012, 2.3MHz core i7 (see Figure 3).

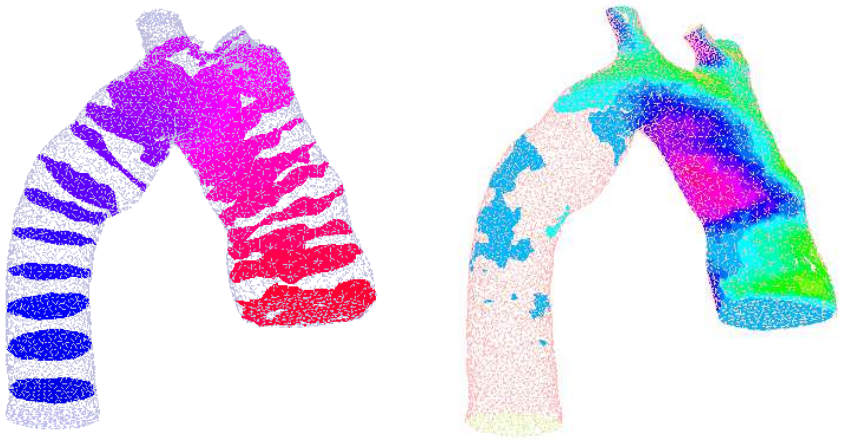

Figure 3 Computation of $[\vec{u}, p]$ with (6.6) for an aorta. Left: Pressure at $t = 0.8$. The compliant walls are updated for graphic visualization of the compliant wall deformation. On the left, the vertical velocity $u_3$ at $t = 0.8$ without graphic enhancement shows also the geometry used for the computation.

### 7.3 Performance on a documented stenosed carotid bifurcation flow

In this section we reproduce the computational results of pulsatile flow in human carotid bifurcation models (see [19–20]). The studies referred to assumed rigid wall arteries. We further extend those results to the full fluid-structure interaction problem with compliant walls.

We have modeled a 10 cm long representative healthy carotid artery bifurcation model, along with 30% and 64% concentrically stenosed models. The common carotid artery has a diameter of 9 mm, while the internal and external carotid arteries have a diameter of 6.8 mm and 5.6 mm, respectively. All artificial boundaries are perpendicular to $x$-axis. Finite-element meshes (coarse discretization $h = 0.2$ mm, 1885 vertices) are shown in Figure 4. Fine discretizations are built with $h = 0.04$ mm resulting roughly in $2 \cdot 10^5$ vertices and one million tetrahedral elements.

First, in order to compare our results with those cited above, we consider $\Sigma$ to be a rigid wall. We also replaced the inlet boundary condition $\int_\Gamma p_\Gamma \widehat{u}_n$ by the velocity profile

$$U_\Gamma = \frac{2\,Q}{A_{\mathrm{CCA}}}\left(1 - \frac{y^2}{R_{\mathrm{CCA}}^2} - \frac{z^2}{R_{\mathrm{CCA}}^2}\right),$$

where $Q$ is the flow rate depicted in Figure 4(right). Spline interpolation is used to fit the pointwise data; traction-free boundary conditions are imposed at the outlet boundaries.

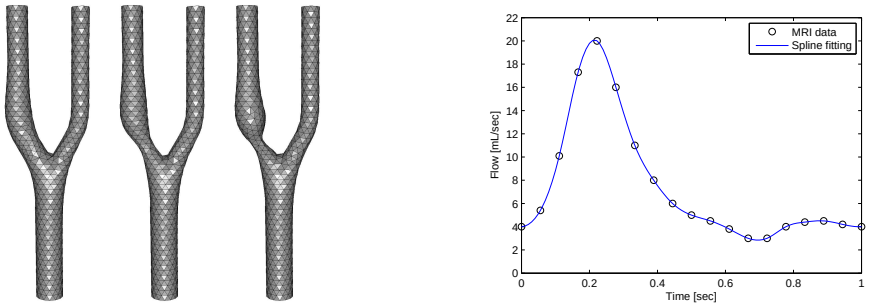


Figure 4 Carotid bifurcation: Healthy (left), 30% (middle), 64% (right) stenosed models (coarse discretization). Flow rate waveform at the common carotid artery inlet.

The initial velocity-pressure field at $t = 0$ is set to be a solution of the Oseen equation. The time step is 0.01. Five cardiac cycles are sufficient to eliminate transient effects caused by initial conditions, and to obtain cyclically repeated flow patterns. For the considered geometries, the inlet flow together with $\nu = 3.5 \cdot 10^{-3}$ Pa·sec and $\rho = 1060\,\mathrm{kg}\cdot\mathrm{m}^{-3}$ result in a Reynolds number of a few hundred; Re at the inflow surface is 357, Re at the 64% stenosed area is 1280. Excellent agreement with the published results was observed in booth magnitude and location of flow patterns.

Now we use (6.6) with $b = 200$ and $\delta t = 0.01$. The geometry is fixed for the numerical simulations but updated for graphic rendering, $\kappa = 100$. We observe that for all three models the maximum positive displacement, i.e. expansion ($\vec{d} \cdot \vec{n} > 0$), is at $t = 0.17$, while the maximum negative displacement, i.e. contraction, is at $t = 0.64$. Figure 5 shows the updated

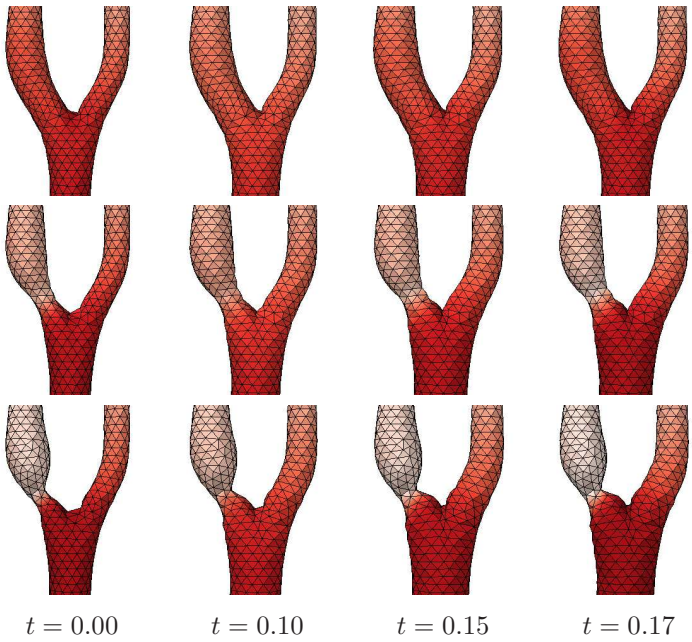


Figure 5 Carotid bifurcation. Arterial displacement during the pre-systolic period; top to bottom: Normal, 30%, 64% stenosis. Dark red color marks regions of higher pressure.

shape of the bifurcation region at four selected phases of the cardiac cycle: $t = 0$, $t = 0.1$, $t = 0.15$ and $t = 0.17$. The red color marks regions with higher pressure. We observe that the healthy artery undergoes a uniform expansion/contraction in the entire domain. For the stenosed arteries, displacements become much larger in the portion of the internal carotid artery below the bifurcation; we identify tiny displacements downstream from the stenosis. More importantly, a steep change in pressure near the stenosis region observed for both 30% and 64% stenosis models will produce an increasing shear stress that could be a reason for arterial rupture.

This paper demonstrates that (6.6) allows physiologically realistic blood flow analysis. A hierarchy of approximations helps reducing the overall computational effort of updating the triangulation at every time step. On the other hand, the method allows us to inspect arterial compliance at arbitrary phases of the cardiac cycle. More importantly, moving the geometry for graphic visualization can be done as a post-processing task, or in parallel.

## References


[1] Begue, C., Conca, C., Murat, F. and Pironneau O., Les equations de Stokes et de Navier-Stokes avec conditions aux limites sur la pression, Nonlinear Partial Differential Equations and Their Applications, H. Brezis, J. Lions (eds.), College de France, Vol. IX, Pitman, RNM Longman, Boston, 1988, 179–264.

[2] Boffi, D. and Gastaldi, L., A finite element approach for the immersed boundary method, *Comput. Struct.*, **81**, 2003, 491–501.

[3] Costabel, M. and Dauge, M., Maxwell and Lamé eigenvalues on polyhedral domains, Université de Rennes I, 2002, preprint.

[4] Costabel, M. and Dauge, M., Singularities of electromagnetic fields in polyhedral domains, Université de Rennes, **1**, 1997, preprint 97-19. http://www.maths.univ-rennes1.fr/∼dauge/

[5] Cottet, G. H., Maitre, E. and Milcent, T., Eulerian formulation and level set models for incompressible fluid-structure interaction, *ESAIM: M2AN*, **42**, 2008, 471–492.

[6] Crosetto, P., Deparis, S., Fourestey, G. and Quarteroni, A., Parallel algorithms for fluid-structure interaction problems in haemodynamics, *SIAM J. Sci. Comput.,* **33**(4), 2011, 1598–1622.

[7] Decoene, A. and Maury, B., Moving meshes with freefem++, *J. Numer. Math.,* **20**(3–4), 2013, 195–214.

[8] De Hart, J., Peters, G., Schreurs, P. and Baaijens, F., A three-dimensional computational analysis of fluid-structure interaction in the aortic value, *J. Biomechanics*, **36**, 2003, 103–112.

[9] Deparis, S., Fernandez, M. A. and Formaggia, L., Acceleration of a fixed point algorithm for fluid-structure interaction using transpiration conditions, *ESAIM: M2AN*, **37**(4), 2003, 601–616.

[10] Hu, F. Q., Li, X. D. and Lin, D. K., Absorbing boundary conditions for nonlinear Euler and Navier-Stokes equations based on the perfectly matched layer technique, *J. Comp. Physics*, **227**, 2008, 4398–4424.

[11] Fernandez, M., Incremental displacement-correction schemes for incompressible fluid-structure interaction, *Numer. Math.*, **123**, 2013, 21–65.

[12] Formaggia, L., Gerbeau, J. F., Nobile, F. and Quarteroni, A., On the coupling of 3D and 1D Navier-Stokes equations for flow problems in compliant vessels, *Comput. Methods Appl. Mech. Engrg.*, **191**, 2001, 561–582.

[13] Formaggia, L., Quarteroni, A. and Veneziani, A., Cardiovasuclar Mathematics, Springer MS&A Series, Springer-Verlag, New York, 2009.

[14] Girault, V. and Glowinski, R., Error analysis of a fictitious domain method applied to a Dirichlet problem, *Japan Journal of Ind. and Applied Math.*, **12**(3), 1995, 487–514.

[15] Girault, V. and Raviart, P. A., Finite Element Method for Navier-Stokes Equations, SCM 5, Springer-Verlag, Berlin, Heidelberg, NewYork, 1986.

[16] Gonzalez, O. and Simo, J. C., On the stability of symplectic and energy-momentum algorithms for nonlinear Hamiltonian systems with symmetry, *Comput. Methods Appl. Mech. Engrg.*, **134**, 1996, 197–222.

[17] Gonzalez, O., Exact energy and momentum conserving algorithms for general models in nonlinear elasticity, *Comput. Methods Appl. Mech. Engrg.,* **190**, 2000, 1763–1783.

[18] Gostaf, K., Pironneau O. and Roux, F. X., Finite element analysis of multi-component assemblies: CAD-based domain decomposition, DDM 14 Proc., to appear.

[19] Marshall, I., Computational simulations and experimental studies of 3d phase-contrast imaging of fluid flow in carotid bifurcation geometries, *J. Magnetic Resonance Imaging*, **31**, 2010, 928–934.

[20] Steinman, D. A., Poepping, T. L., Tambasco, M., et al., Flow patterns at the stenosed carotid bifurcation: Effect of concentric versus eccentric stenosis, *Annal. Biomedical Engineering*, **28**, 2000, 415–423.

[21] Guermond, J. L., Minev, P. and Shen, J., An overview of projection methods for incompressible flows, *Comput. Methods Appl. Mech. Engrg.*, **195**(44–47), 2006, 6011–6045.

[22] Heil, M., Hazel, A. and Boyle, J., Solvers for large-displacement fluid-structure interaction problems: Segregated versus monolithic approaches, *Comput. Mech.*, **43**, 2008, 91–101.

[23] Le Tallec, P., Fluid structure interaction with large structural displacements, *Comput. Methods Appl. Mech. Engrg.*, **190**, 2001, 3039–3067.

[24] Nobile, F. and Vergara, C., An effective fluid-structure interaction formulation for vascular dynamics by generalized robin conditions, *SIAM J. Sci. Comp.*, **30**(2), 2008, 731–763.

[25] Pares, C., Un traitement faible par élément finis de la condition de glissement sur une paroi pour les équations de Navier-Stokes, *C. R. Acad. Sci. Paris Sér. I Math.*, **307**, 101–106, 1988.

[26] Peskin, C., The immersed boundary method, *Acta Numerica*, **11**, 2002, 479–517.

[27] Peskin, C. and McQueen, D., A three dimensional computational method for blood flow in the hearth-I, Immersed elastic fibers in a viscous incompressible fluid, *J. Comput. Phys.*, **81**, 1989, 372–405.

[28] Pironneau, O., Finite Element Methods for Fluids, Wiley, New York, 1989.

[29] Pironneau, O., Conditions aux limites sur la pression pour les équations de Stokes et de Navier-Stokes, *C. R. Acad. Sci. Paris Sér. I Math.*, **303**(9), 1986, 403–406.

[30] Pironneau, O. and Tabata, M., Stability and convergence of a Galerkin-characteristics finite element scheme of lumped mass type, *Int. J. Numer. Meth. Fluids*, **64**, 2010, 1240–1253.

[31] Rannacher, R., Incompressible Viscous Flow, Encyclopedia Mecanicae, E. Stein (ed.), Wiley, New York, 2004.

[32] Rappaz, J. and Flotron, S., Numerical conservation schemes for convection-diffusion equations, to appear.

[33] Si, Z. Y., Second order modified method of characteristics mixed defect-correction finite element method for time dependent Navier-Stokes problems, *Numer. Algor.*, **59**, 2012, 271–300.

[34] Tambaca, J., Canic, S., Kosor, M., et al., Mechanical Behavior of Fully Expanded Commercially Available Endovascular Coronary Stents, *Tex Heart Inst. J.*, **38**(5), 491–501, 2011.

[35] Thiriet, M., Biomathematical and biomechanical modeling of the circulatory and ventilatory systems, Control of Cell Fate in the Circulatory and Ventilatory Systems, Vol. 2, Math and Biological Modeling, Springer-Verlag, New York, 2011.

[36] Usabiaga, F., Bell, J., Buscalioni, R., et al., Staggered schemes for fluctuating hydrodynamics, *Multiscale Model Sim.*, **10**, 2012, 1369–1408.

[37] Vignon-Clementel, I., Figueroa, A., Jansen, K. and Taylor, C. A., Outflow boundary conditions for three-dimensional finite element modeling of blood flow and pressure in arteries, *Comput. Methods Appl. Mech. Engrg.*, **195**, 2006, 3776–3796.